Deciphering the Interplay between Local and Global Dynamics of Anodic Metal Oxidation

Aleksei Makogon, Jean-Marc Noël, Frédéric Kanoufi, Viacheslav Shkirskiy*

Université Paris Cité, ITODYS, CNRS, 75013 Paris, France

Abstract

The stark difference between global and local metal oxidation dynamics underscores the need for methodologies capable of performing precise sub-µm-scale and wide-field measurements. In this study, we present Reflective Microscopy as a tool developed to address this challenge, illustrated by the example of chronoamperometric Fe oxidation in NaCl solution. Analysis at a local scale of 10s of µm has revealed three distinct periods of Fe oxidation: the initial covering of the metal interface with a surface film, followed by the electrochemical conversion of the formed surface film, and finally, the in-depth oxidation of Fe. In addition, thermodynamic calculations and the quantitative analysis of changes in optical signal (light intensity), correlated with variations in refractive indexes, suggests the initial formation of maghemite, followed by its subsequent conversion to magnetite. The reactivity maps for all three periods are heterogeneous, which can be attributed to the preferential oxidation of certain crystallographic grains. Notably, at the global scale of 100s of µm, reactivity initiates at the electrode border and progresses towards its center, demonstrating a unique pattern that is independent of local metal structure. This finding underscores the significance of simultaneously employing sub-µm-precise, quantitative and wide-field measurements for a comprehensive description of metal oxidation processes.

Keywords: Optical Microscopy, Metal Oxidation, Film Growth, Global vs Local Dynamics, Iron

Corresponding author: viacheslav.shkirskiy@cnrs.fr

TOC

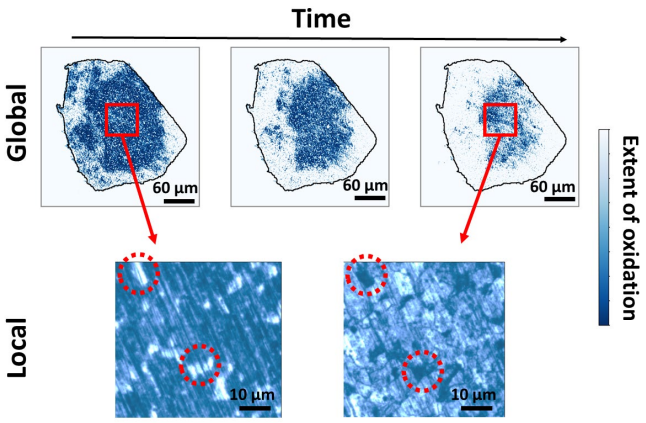

https://doi.org/10.26434/chemrxiv-2023-stbm1-v3 **ORCID:** https://orcid.org/0000-0003-4289-9678 Content not peer-reviewed by ChemRxiv. **License:** CC BY-NC-ND 4.0

Introduction

Recent advancements in the development and application of local probe techniques have highlighted the pronounced heterogeneity in metal oxidation, an attribute that is discernible even within pure metal phases.[1–5] The isolation of individual grains and grain boundaries within a nanodroplet electrochemical cell - also known as Scanning Electrochemical Cell Microscopy (SECCM) - demonstrated that these grain boundaries exhibit the most substantial electrochemical activity within a polycrystalline metal structure.[6–11] The rate of oxidation was shown to be linked with the increase in grain boundary energy, the density of fractured bonds at the grain boundary plane, and the energy of metal oxidation on individual facets.[6,7,12,13] This discovery presents a significant challenge to conventional methods of interpreting global electrochemical measurements, which have often been premised on the assumption of uniform metal reactivity.[14–17] Simultaneously, it is important to note that global reactivity cannot be solely inferred from the measurements of isolated nanoscopic areas. This is due to the cooperative interplay between metal heterogeneities resulting from the formation of extensive galvanic couplings,[18,19] the diffusive exchange of dissolved species,[20–23] among other factors.[24] As a result, conducting a comprehensive analysis of metal oxidation reactions necessitates the formulation and implementation of methodologies—ones that balance both highly precise quantitative measurements, capable of delving into nanometer-scale intricacies, and wide-field measurements that can cover expanses up to the millimeter range.[25] To tackle this challenge and demonstrate the merits of dual-pronged, precision-focused quantitative and wide-field, in-situ measurements in the realm of metal oxidation, we utilized Reflective Microscopy (RM).

RM is a label-free optical imaging technique that leverages local changes in the refractive index at the image interface to elucidate various (electro-)chemical phase transformations.[26–35] Garcia et al.[22,28,36] demonstrated that, in the context of metal oxidation, light intensities correlated ex-situ with surface analysis techniques can indicate phenomena such as de-alloying, subsurface corrosion, etching, or pitting in Al alloys. Recently, optical models utilizing light interference at oxidized metal interfaces have shown that variations in optical intensities can quantitatively relate to the thickness (to nanometer precision) and composition of surface films.[23,25,26,37] These parameters are central to our understanding of metal passivation and corrosion protection. When augmented with machine vision methodologies,[38,39] RM evolves into an automated, robust, and flexible approach. Compared to traditional *in-situ* methods for characterizing passive films, such as scanning tunneling microscopy (STM), transmission electron microscopy (TEM), X-ray photoelectron spectroscopy (XPS), and others, it is significantly less costly and time-consuming.[25,40–45] The versatility and efficacy of RM approach are further demonstrated in this study through the examination of corrosion in pure polycrystalline Fe metal in a NaCl medium.

With a primary focus on illustrating the methodological approach of combined quantitative global and local observations, we selected Fe as our subject, given its status as one of the most extensively

https://doi.org/10.26434/chemrxiv-2023-stbm1-v3 **ORCID:** https://orcid.org/0000-0003-4289-9678 Content not peer-reviewed by ChemRxiv. **License:** CC BY-NC-ND 4.0

studied systems in the field of corrosion.[41–45] Unlike previous studies,[22,28,36] our work focuses on quantitative aspects, establishing a direct link between the variations in local light intensities and the global electrical currents – a methodological breakthrough enabled by recent advancements in optical modeling.[23,25,26,37] In scenarios where RM quantification does not suffice, our efforts were centered on finding ways to address these limits and cautioning against its inappropriate application. Moreover, we have developed and publicly shared (https://doi.org/10.5281/zenodo.8341764) an automated data processing procedure that reproduces all images and substantiates all the conclusions drawn in this manuscript. Overall, this study highlights the importance of a dual-pronged approach in electrochemical research, presenting a quantitative framework for analyzing optical signals.

Results and Discussion

Chronoamperometric Analysis of Fe Oxidation: The Three Periods

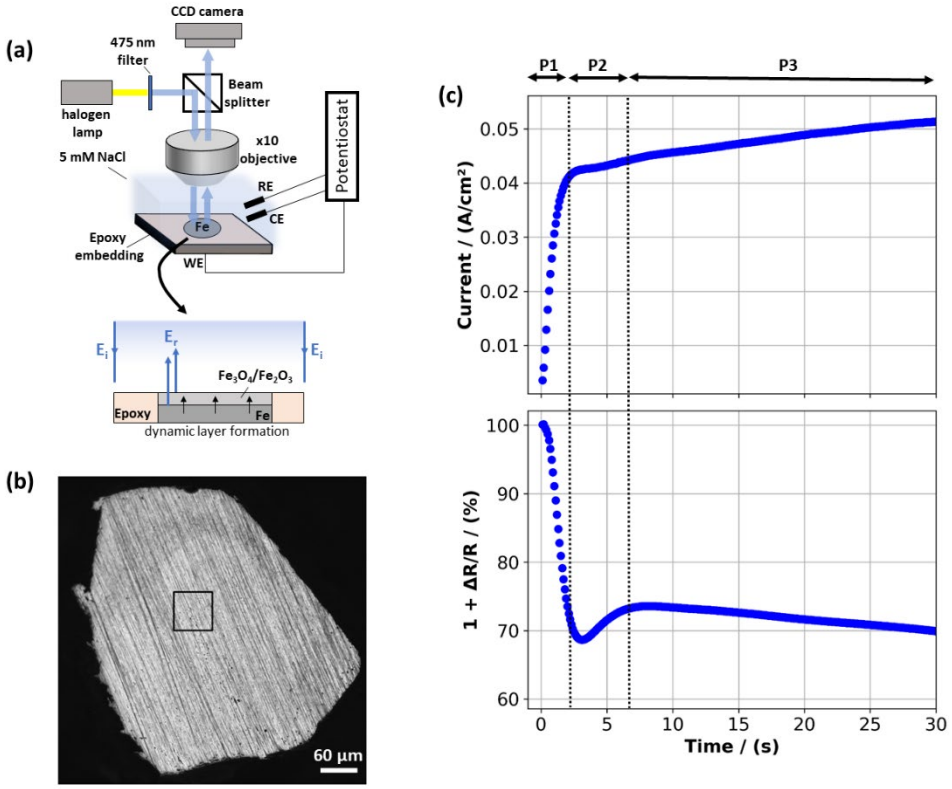

Fig. 1 (a) *Schematic illustration of the RM approach, coupled with electrochemical characterization of a millimeter-sized Fe electrode. The top part of the figure provides a general view of the apparatus, while the bottom part illustrates the optical signal generation. Incident light (E_i), filtered at 475 nm, is focused on the metal interface during potentiostatic oxidation. The collected light includes contributions from the reflected light (E_r) from the surfaces of Fe oxides and the metal, which is proportional to the thickness of surface films and their chemical composition. (b) Optical image of the polished Fe interface, the back square corresponding to the surface optically monitored in Fig. 2c. (c) Plots of electrochemical current (top) and averaged normalized reflectivity (bottom) as a function of*

https://doi.org/10.26434/chemrxiv-2023-stbm1-v3 **ORCID:** https://orcid.org/0000-0003-4289-9678 Content not peer-reviewed by ChemRxiv. **License:** CC BY-NC-ND 4.0

time during potentiostatic metal oxidation performed at -0.3 V vs. 3.4 M KCl Ag/AgCl (or +0.1 V vs. the OCP value) in a 5 mM NaCl solution. Dotted lines highlight the three distinct periods (P1, P2, and P3) observable from both the electrochemical and optical data. This experiment was repeated 4 times in total.

We coupled a conventional three-electrode electrochemical setup with in-situ RM observations to aid in interpreting the global electrochemical current during potentiostatic Fe oxidation (Fig. 1a). Before Fe oxidation, the Fe electrode was polished with 1200 grit SiC, thereby creating a surface roughness of 5 µm. This process rendered visible, optically discernable directional polishing lines, as illustrated in Fig. 1b. This procedure was carried out deliberately to investigate any possible correlation between the direction of the polishing lines and the propagation pattern of corrosion. To ensure complete visibility under an optical microscope (Fig. 1b), the Fe electrode was designed with a surface area of 0.0015 cm^2, comparable to standard sizes in macroscale electroanalytical analysis. This setup facilitated direct correlation between the measured electrical current and the averaged optical reflectivity. The sample was then positioned in a corrosive electrolyte of 5 mM NaCl (neutral pH) within the opto-electrochemical setup. The OCP was measured for 5 minutes, yielding a value of -0.4 V vs 3M Ag/AgCl. During this period, no variations in the optical intensity were observed. An anodic potential of +0.1 V vs OCP was then applied for approximately 3 minutes. During this period, we recorded two independent measurements: the global electrochemical current from the potentiostat and the dynamic optical images of the Fe surface. The latter was achieved through a ×10 water immersion objective under illumination with blue light (490 nm) collected onto a CCD camera. Both electrochemical and optical measurements were recorded at an identical acquisition rate of 10 Hz. This experiment was repeated 4 times in total (with the whole dataset available in the Zenodo repository (https://doi.org/10.5281/zenodo.8341764) and complementary experimental details available in Supplementary Information(SI)), yielding identical trends that we analyzed in detail based on a typical example discussed below.

First, we examine the global electrical current and averaged optical signal, expressed as the evolution of averaged normalized intensity (Fig. 1c). Both curves reveal three distinct periods.

Period 1 (P1) initiates immediately upon potential imposition and lasts approximately 2-3 s. This period is characterized by a sudden current density increase up to 0.04 A/cm^2, coupled with an abrupt decrease in surface reflectivity, by approximately 30 %. These observations indicate surface-controlled oxidation, leading to the formation of surface films. Extensive previous research using *in-situ* STM[41–45] and *in-situ* synchrotron X-ray diffraction[46,47] has suggested that the surface film formed is crystalline and comprises γ-Fe_2O_3 (maghemite) and Fe_3O_4 (magnetite) compounds, dependent on the pH and extent of Fe oxidation. For guidance in identifying these species, refer to Fig. 2b, which displays the potential-pH relationship of Fe, calculated using the latest thermodynamic data on Fe corrosion

https://doi.org/10.26434/chemrxiv-2023-stbm1-v3 **ORCID:** https://orcid.org/0000-0003-4289-9678 Content not peer-reviewed by ChemRxiv. **License:** CC BY-NC-ND 4.0

products. Details on the derivation of this figure are available in the SI. It shows that at neutral pH, maghemite should form with a concurrent acidification of the environment due to water hydrolysis:

$$2Fe + 3H_2O \leftrightarrow Fe_2O_3 + 6H^+ + 6e^- \quad (1).$$

Upon analyzing raw optical images captured on a scale of 10s of µm, as demonstrated in Fig. 2c, a distinct heterogeneous darkening pattern emerges at the metal interfaces within the 0-s to 2-s timeframe. This pattern corresponds to the localized extent of surface oxidation. Intriguingly, the direction of polishing seems to exert minimal influence on this pattern's distribution. Areas exhibiting a polygonal shape and sizes smaller than 10 µm (circled for emphasis) notably sustain a lighter hue, which closely resembles the metal crystallographic texture.[6–11] It is crucial to mention that our experiment utilized pure Fe, effectively eliminating chemical heterogeneities as a potential explanation for the observed patterning.

Period 2 (P2) follows immediately and lasts about 5 seconds. It is discernable by a slight decrease in current density (Fig. 1c, top graph, P2) and a marked increase in normalized reflectivity, from approximately 70 % to about 75 % (Fig. 1c, bottom graph, P2). An assessment of localized raw optical images at the 7-s mark, as depicted in Fig. 2c, reveals a notable contrast shift. Areas that appeared bright in the 2-s image have since darkened, while areas that were initially dark have become noticeably brighter. A modest reduction in current density at this point could be indicative of cathodic (reduction) processes. Examining the potential vs pH diagram in Fig. 2b suggests that a shift in local pH, as a result of Eq. 1, might prompt the reduction from the maghemite Fe(III) phase to the mixed Fe(II)/Fe(III) magnetite phase at a set potential of -0.3 V (highlighted by an arrow in Fig. 2b), consistent with the conditions of our experiment:

$$3Fe_2O_3 + 2H^+ + 2e^- \leftrightarrow 2Fe_3O_4 + H_2O \quad (2).$$

The simulated optical response in Fig. 2a concurs with this explanation. Given the similar densities of maghemite and magnetite ($\rho_{Fe_2O_3} = 4.9$ g/cm^3 and $\rho_{Fe_3O_4} = 5.0$ g/cm^3), their interconversion would not yield a substantial alteration in the thickness of the surface layer. At the same time, for identical thickness of surface films, the maghemite layer absorbs more light than the magnetite layer, therefore causing the reflectivity to increase during the described surface layer transformation (indicated with the dashed arrow in Fig. 2a).

https://doi.org/10.26434/chemrxiv-2023-stbm1-v3 **ORCID:** https://orcid.org/0000-0003-4289-9678 Content not peer-reviewed by ChemRxiv. **License:** CC BY-NC-ND 4.0

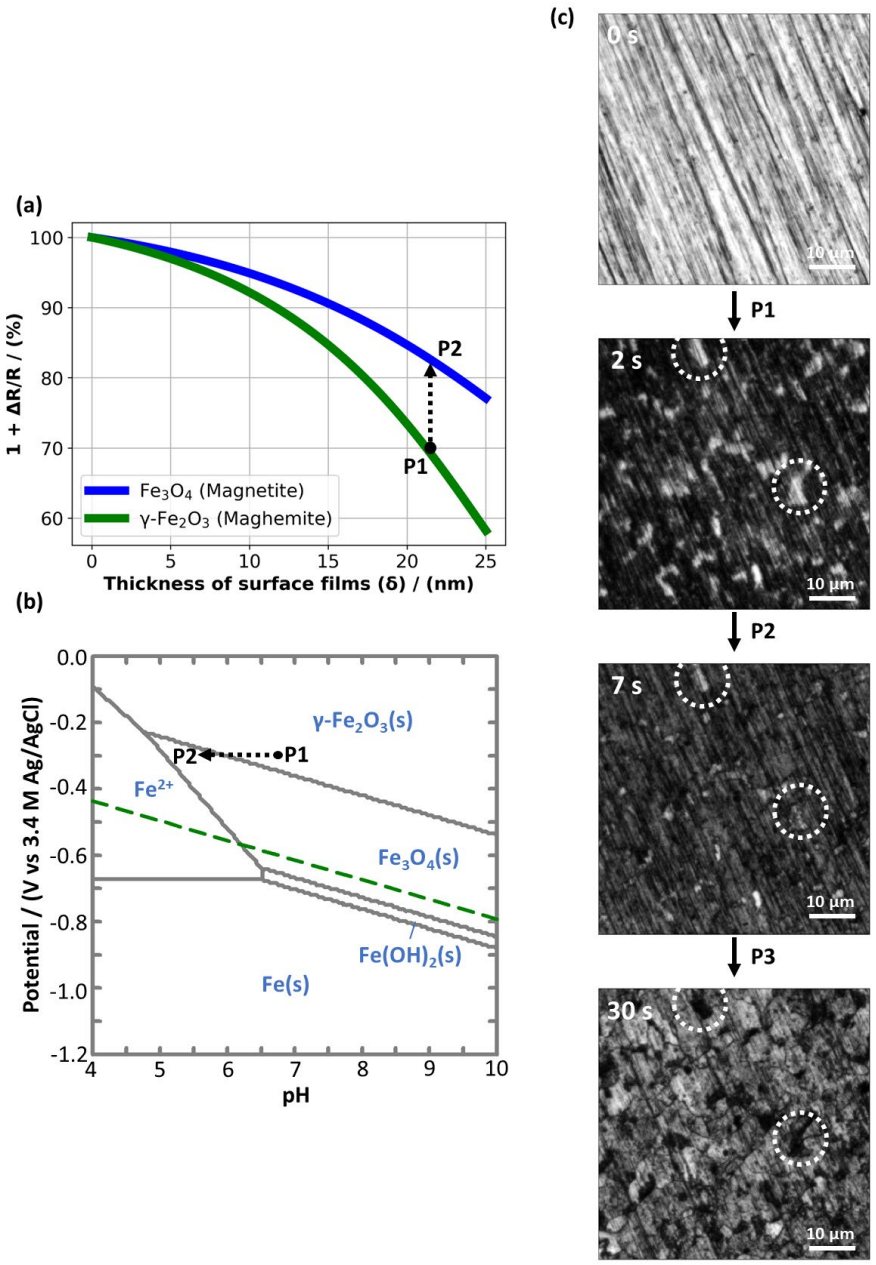

Fig. 2 *(a) Evolution of normalized reflectivity as a function of surface film thickness for magnetite (blue line) and maghemite (green line), estimated using the Fresnel equation. The input values of refractive indices (n) for simulations are as follows (for λ = 490 nm):* $n_{Fe} = 1.06 + 4.99i$, $n_{Fe_3O_4} = 2.3$, $n_{\gamma-Fe_2O_3} = 2.6$, $n_{H_2O} = 1.3$[48–54] *with more details reported in SI. (b) A potential-pH diagram for Fe, calculated using the HYDRO Medusa Chemical Equilibrium Software*[55] *with details reported in SI. The green dotted line represents proton reduction. The dotted arrow in both (a) and (b) illustrates the proposed transition between Periods 1 (P1) and 2 (P2) observed in the chronoamperometric experiment. (c) Optical images of the Fe surface (see inset in Fig. 1b) taken at 0, 2, 7, and 30 seconds into the chronoamperometric process, showcasing the transition between P1, P2, and P3. The white dotted circles are depicted over identical locations to serve as visual references.*

https://doi.org/10.26434/chemrxiv-2023-stbm1-v3 **ORCID:** https://orcid.org/0000-0003-4289-9678 Content not peer-reviewed by ChemRxiv. **License:** CC BY-NC-ND 4.0

Period 3 commences around the 7-second mark, extending until the culmination of the polarization experiment. This phase exhibits a consistent increase in current, as seen in Fig. 1c. Local optical image, captured at the 30-second interval and presented in Fig. 2c, demonstrates a marked darkening of the initially bright sections on the Fe surface. These sections were first observed in the 2- and 7-second snapshots (indicated by white circles for easy reference). Contrarily, the areas that were dark in the 2- and 7-second images exhibit increased reflectivity. This phenomenon, as discussed earlier, could potentially result from the transformation of the initially formed maghemite layer into magnetite on the surface. Interestingly, the reflectivity enhancement covers a much larger area than the localized surface darkening. However, despite the broadened region of increased brightness, the total reflectivity diminishes (Fig. 1c, bottom graph). This observation emphasizes that, in terms of absolute values, the darkening effect is dominant. Its confined distribution suggests a highly localized metal oxidation, which could be indicative of pits.

We wish to emphasize that, although the current reached significant values (ca. 0.05 A/cm^2) by the end of the experiment, the total charge consumed was only around 1.3 C/cm^2, given the brief duration (30 s) of the chronoamperometric test. This translates, on average, to the formation of surface films of about 300 nm (detailed in Eq. 3). Considering the density difference between Fe (ρ_{Fe}=7.8 g/cm^3) and Fe oxides (assumed as $\rho_{Fe_2O_3} = 4.9$ g/cm^3), the height of the interface should increase by approximately 150 nm at the end of the experiment. With the high x10 magnification of our objective lens, such a minor shift in focus distance should not impact our optical measurements, which would need to be in the µm range to be noticeable.

In the subsequent sections, we will describe the spatial distribution of reflectivity alterations for the entirety of oxidized Fe interface and establish a quantitative correlation between current and optical intensities. This validation confirms the initial assignments of the chemical composition of the passive layer, identified as being composed of maghemite and magnetite, initially based on literature review[41–47] and the potential-pH diagram in Fig. 2b. We emphasize that we did not conduct *in-situ* STM, *in-situ* synchrotron X-ray diffraction, or other sophisticated analyses, as these have already been performed in the literature.[41–47] Instead, we demonstrate how the simple yet data-rich RM approach, based on refractive index analysis, can facilitate the chemical identification of a nanometer-thick passive layer.

Period 1: Initial Formation of Surface Films on Fe Interface

Fig. 3a illustrates the spatial distribution of normalized optical intensities across the entire surface of the Fe electrode during the initial stages of chronoamperometry, reflecting the propagation of surface film formation. To improve contrast and enhance visual representation, light intensities of frame (N) were normalized by frame (N-10), as indicated by the subscript ΔR_{10} throughout the manuscript. This normalization method is particularly useful for highlighting subtle differences in a series of images and is consistently applied to all image series below.

https://doi.org/10.26434/chemrxiv-2023-stbm1-v3 **ORCID:** https://orcid.org/0000-0003-4289-9678 Content not peer-reviewed by ChemRxiv. **License:** CC BY-NC-ND 4.0

Upon examining the images of the entire Fe interface at 0.8 s, 1.0 s, and 1.5 s in Fig. 3a, it is apparent that the darkening of the metal interface starts preferentially at the edge of the Fe electrode and then propagates towards the center of the electrode. It is important to note that the initial image at 0 s (not displayed here but available in the Zenodo repository) exhibits a completely white appearance. This corresponds to 100% of $1+\Delta R_{10}/R$, indicating that there were no observable changes prior to the application of chronoamperometry, which commenced at the 0-second mark. The areas outside of the electrode are filled with an epoxy resin where no changes occur, hence the normalized reflectivity remains at 100%, as indicated by the white color in the chosen color scheme of Fig. 3a. The surface darkening towards the electrode center is not discernible on the 10 µm scale from the image insets in Fig. 2c and is only noticeable due to the observation of the entire active area at the scale of hundreds of µm. This observation suggests that the kinetics of localized oxidation are significantly influenced by the electrode's border at the mm scale, apart from the influence of the Fe interface's crystallographic structure at the µm scale. It should be noted that the border of the Fe electrode in Fig. 3a, as well as in all subsequent electrode images in Figs. 4 and 5a, is distinctly defined, exhibiting an abrupt color change. This indicates the absence of confined spaces at the electrode border, allowing us to rule out crevice corrosion on the electrode edges.

Assuming that the reflectivity change obeys the Fresnel law – that is, it is directly related to the formation of surface films – the first derivative of the averaged reflectivity change should be proportional to the current density. We considered only data from the initial 2 seconds, during which the surface films were presumed to be predominantly composed of maghemite, as discussed in the previous section. As shown in Fig. 3b, the current density and optical reflectivity - both independent measurements - indeed share a relationship during the initial period of oxidation. Subsequently, we used current density values to recalculate the average thickness of maghemite surface films as function of time ($\delta(t)$), assuming 100% Faradaic efficiency:

$$\delta(t) = {Q(t)M_{Fe_2O_3}}\Big/{2nF\rho_{Fe_2O_3}} \quad (3),$$

where $Q(t)$ is the cumulative charge normalized by the electrode surface area of 0.0015 cm^2, $M_{Fe_2O_3}$ is the molar mass of maghemite (160 g/mol), n is the number of electrons per consumed Fe metal (n=3), F is the Faraday constant (96500 C/mol) and $\rho_{Fe_2O_3}$ is the density of maghemite layer (4.9 g/cm^3). Factor 2 was added to account the stoichiometry between Fe and Fe_2O_3 in Eq. 1. The evolution of surface films thus calculated is plotted against the change in normalized reflectivity in Fig. 3c (dotted line). The solid lines in Fig. 3c shows the theoretical optical response for a maghemite and magnetite layers, replicated from Fig. 2a.

https://doi.org/10.26434/chemrxiv-2023-stbm1-v3 **ORCID:** https://orcid.org/0000-0003-4289-9678 Content not peer-reviewed by ChemRxiv. **License:** CC BY-NC-ND 4.0

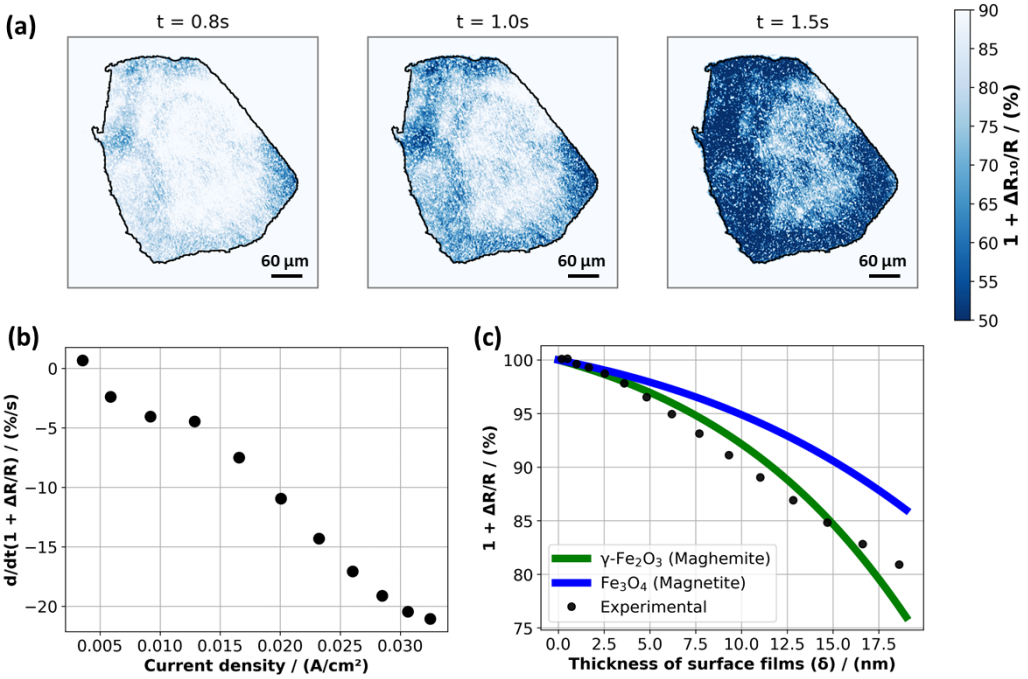

Fig. 3 *Analysis of Fe reactivity during P1. (a) Maps of normalized reflectivities after 0.8, 1.0, and 1.5 seconds of chronoamperometry. Reflectivity of frame (N) is normalized by the reflectivity of frame (N-10), as denoted in the subscript of the reflectivity change. The black line, which is placed for visual reference, underlies the area of the Fe electrode. (b) First derivative of averaged normalized reflectivity plotted as a function of electrochemical current density. (c) Experimental optical and electrochemical data, recalculated as the thickness of surface films using Eq. 3 (represented by black dots), overlaid with theoretical curves of normalized reflectivity for maghemite (green line) and magnetite (blue line), replicated from Fig. 2a.*

Among the two theoretical curves presented in Fig. 3c, the curve corresponding to maghemite shows a superior correlation with the experimental data derived from Eq. 3. This finding is consistent with thermodynamic calculations and corroborated by extensive previous research.[41–47] The minor divergence between the curve corresponding to maghemite and experimental data could arise due to the surface film already transitioning from maghemite to magnetite, as slight surface brightening can be noticed on the peripheries of the 1.5 s image in Fig. 3a. Another possible source of this deviation could be attributed to the initial Fe surface not being flawlessly flat. Instead, it exhibits an approximate 5 µm roughness, akin to the roughness of the applied polishing pad. As a result, the optical simulations, ideally meant for flat surfaces, might diverge from the measured data[56,57] and the current density, since the geometric surface area was utilized for current density calculations. Despite these oversimplifications, the congruence between the completely independent electrochemical and optical measurements strengthens the validity of the estimated chemical composition. This also

https://doi.org/10.26434/chemrxiv-2023-stbm1-v3 **ORCID:** https://orcid.org/0000-0003-4289-9678 Content not peer-reviewed by ChemRxiv. **License:** CC BY-NC-ND 4.0

illustrates how an optical Fresnel model, based on refractive index analysis, can be effectively correlated with calculations of surface film compositions derived from Faraday's law.

Period 2: Transformation and Evolution of Surface Films

During period 2, the surface brightens, as can be observed from Fig. 4, an effect associated with the transformation of maghemite to magnetite in the surface layer. The normalized reflectivity starts to increase at the border of the Fe electrode in the image at 2.5 s, which rapidly propagates towards the center at 3.0 s and 3.5 s (Fig. 4). This transformation from maghemite to magnetite is fundamentally electrochemical, but its rate should be strongly influenced by local pH as suggested by the potential vs pH diagram in Fig. 2b. In turn, the local pH should be dictated by the local oxidation rate of metallic Fe (Eq. 2). Consequently, despite its dependence on pH, the observed pattern of normalized reflectivity change - beginning at the border and gradually spreading towards the center of the electrode - likely mirrors the gradient of electrochemical activity, similar to the variations in optical intensity witnessed during period 1.

Having demonstrated the adequacy of estimating the average surface film thickness in Eq. 5 in the preceding section, we can reframe it to estimate the average flux of H^+ (J_{H^+}). By factoring in the stoichiometry from Eq. 3, we can express J_{H^+} as follows:

$$J_{H^+} = {}^{i}/_{F} \tag{6},$$

where i represents the electrochemical current density. Applying the first Fick's law in a one-dimensional scenario,[58] the surface pH can be formulated under the steady-state assumption as:

$$pH_{surf} = -lg\left({}^{J_{H^+}}/_{D_{H^+}}\, x + C_{bulk}\right) \tag{7},$$

where D_{H^+} is the diffusion coefficient of H^+ ($9.3 \cdot 10^{-9}$ m^2/s),[58] x signifies the thickness of the diffusion layer (presumed to be 150 nm, a typical measure for a stagnant electrolyte under natural convection conditions),[59,60] and C_{bulk} represents the bulk concentration of H^+ (considered as 10^{-7} M). According to Eq. 7, the observed current increase from 0.001 to 0.04 A/cm^2 during the initial 0.1-2.5 s (during P1) of the experiment could result in a pH decrease to values between 5.7 and 4.2.

https://doi.org/10.26434/chemrxiv-2023-stbm1-v3 **ORCID:** https://orcid.org/0000-0003-4289-9678 Content not peer-reviewed by ChemRxiv. **License:** CC BY-NC-ND 4.0

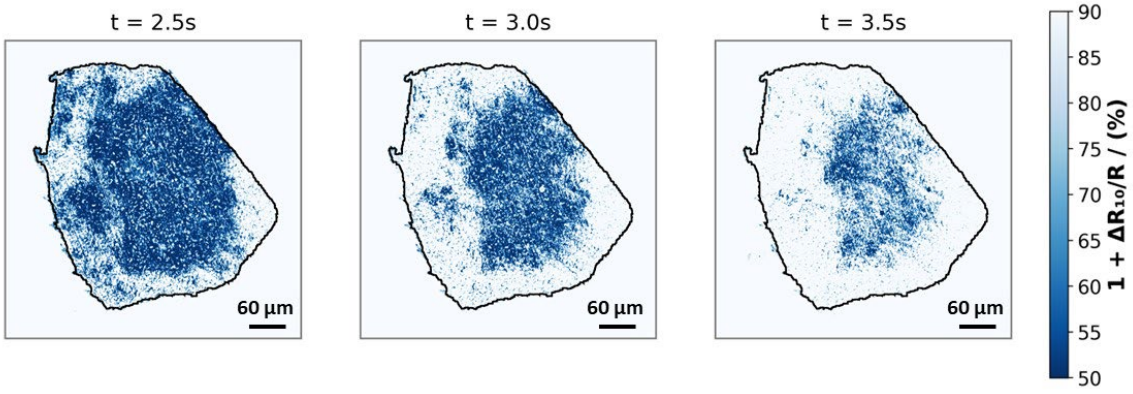

Fig. 4 *Analysis of Fe reactivity during P2. This figure displays maps of normalized reflectivities at 2.5, 3.0, and 3.5 seconds into the chronoamperometry. The reflectivity of each frame (N) is normalized by the reflectivity of the preceding frame (N-10), as indicated in the subscript of the reflectivity change. The black line, which is placed for visual reference, underlies the area of the Fe electrode.*

The decline in pH to around 5 aligns with the proposed transition from P1 to P2, as illustrated in the potential-pH diagram in Fig. 2b. This observation suggests that the proposed transition may begin as early as 0.1 seconds into the chronoamperometry process, as previously discussed. Notably, the slight surface brightening indicative of magnetite formation is observable at the peripheries in the 1.5-second image shown in Fig. 3a. A further decline in pH to values below 5 could potentially instigate the subsequent shift into the Fe^{2+} region, thereby causing the dissolution of surface films. While the scenario seems thermodynamically feasible, the evident darkening at the metal interface points towards negligible metal dissolution. This could denote a kinetic hindrance in the dissolution process and/or elevated local concentrations of Fe ions, which could foster the formation of surface films.

Period 3: Progressive In-Depth Metal Oxidation

Fig. 5a presents the spatial distribution of the evolution of normalized reflectivity during the last stage (t > 7 s) of chronoamperometry application. In this period, the changes are more subtle, providing a milder contrast between different areas of the electrode. Consequently, the scale of the color scheme was adjusted with a reflectivity of 100%, representing the epoxy surface surrounding the Fe electrode, depicted in light blue color.

https://doi.org/10.26434/chemrxiv-2023-stbm1-v3 **ORCID:** https://orcid.org/0000-0003-4289-9678 Content not peer-reviewed by ChemRxiv. **License:** CC BY-NC-ND 4.0

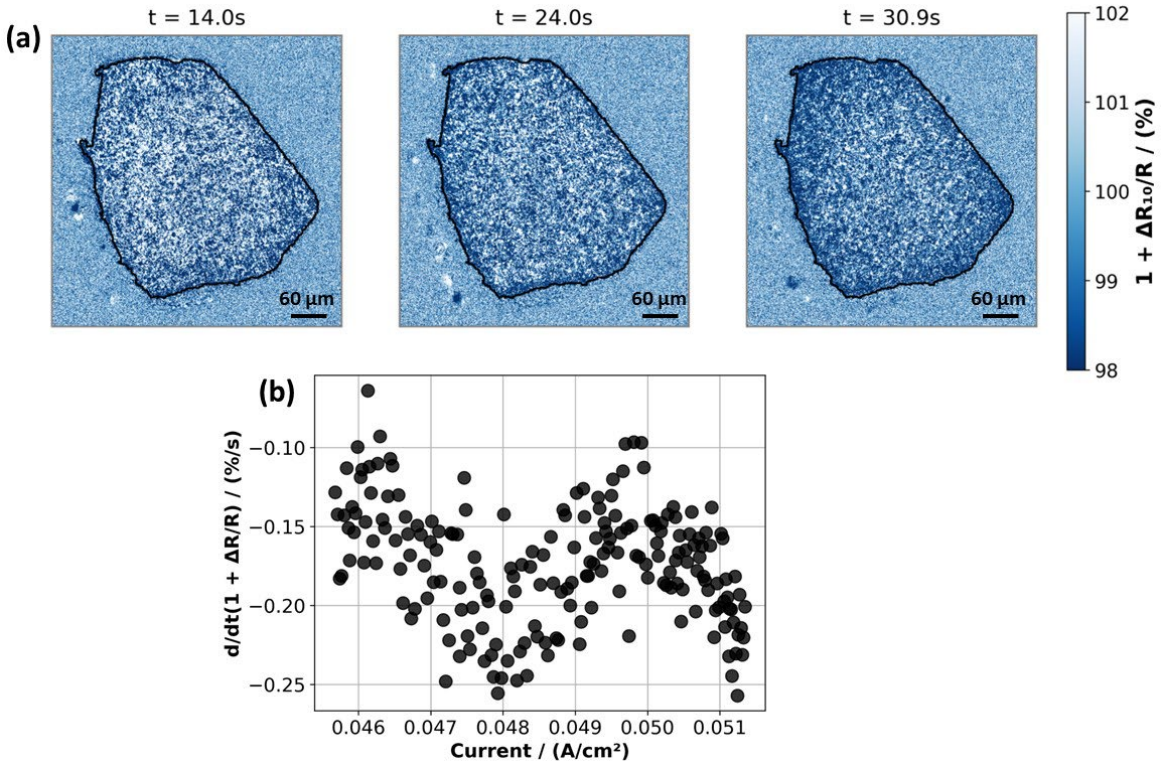

Fig. 5. *Analysis of Fe reactivity during P3. (a) Maps of normalized reflectivities taken at 14.0, 24.0, and 30.9 seconds into the chronoamperometry process. The reflectivity of each frame (N) is normalized by the reflectivity of the preceding frame (N-10), as indicated in the subscript of the reflectivity change. The black line, which is placed for visual reference, underlies the area of the Fe electrode. (b) The first derivative of averaged normalized reflectivity is plotted as a function of the electrical current density.*

The darkening of the Fe electrode becomes apparent in the images taken at 14.0 s, 24.0 s, and 30.9 s (Fig. 5a). Notably, we also observe macroscopically that the darkening tends to initiate preferentially at the edge of the Fe electrode, gradually advancing towards the electrode's center. As discussed earlier, the darkening of the Fe interface during this period indicates localized in-depth progression that can exceed the penetration depth of light into the surface film (several hundreds nm).[31] In theory, no changes in visible light should be discernible. However, the subtle changes observed in this case could be attributed to the fact that on certain grains, in-depth corrosion does not surpass the light penetration depth, rendering optical detection still feasible.

The proportion of the current resulting from the oxidation of these grains should be marginal compared to the typically in-depth, pit-like corrosion.[61] Therefore, only a minor correlation should exist between the current density and changes in normalized reflectivity. This hypothesis is validated in Fig. 5b, where we plot the first derivative of the changes in averaged normalized reflectivity against the current density, similar to what was done for period 1. As anticipated, a minor correlation was detected, observable through periodic intensity fluctuations in the range of 0.15% s^{-1} (as shown on the

https://doi.org/10.26434/chemrxiv-2023-stbm1-v3 **ORCID:** https://orcid.org/0000-0003-4289-9678 Content not peer-reviewed by ChemRxiv. **License:** CC BY-NC-ND 4.0

y-axis in Fig. 5b). However, this observed variation is characteristically noisy and could be confounded by the stability of the light source at these signal levels, thereby complicating the interpretation of data for quantitative analysis. In line with the above discussions, these perceived periodic variations may signify subtle transformations in the surface film and/or film dissolution due to localized pH acidification.

In summary, observations made on a larger scale of hundreds of μm enabled us to probe the electrochemical dynamics of reactivity that begins at the electrode border and advances towards the center. We reiterate that the border of the Fe electrode, as seen in Fig. 3a and in all subsequent electrode images in Figs. 4 and 5a, is distinctly defined by an abrupt color change between the epoxy resin and the metal substrate. This distinct delineation indicates the absence of confined spaces at the electrode border, enabling us to rule out the possibility of crevice corrosion along the electrode edges. Intriguingly, the direction of macroscale metal oxidation remained unaffected by the directional polishing lines present on the Fe substrate after sample preparation. While it is anticipated that electrode reactivity begins at the edge because of its increased accessibility,[62–65] this detail is frequently omitted in discussions on local metal oxidation and in considerations of polycrystalline metal surface reactivity in macroscale electroanalysis.[1–5,14–17] Our study offers direct evidence that enhanced reactivity at the electrode edge substantially influences grain-dependent localized current densities and cannot be overlooked.

Conclusions

We investigated the anodic oxidation of polycrystalline pure Fe metal in 5 mM NaCl using a dual-pronged, precision-focused, and wide-field opto-electrochemical RM approach. This was done to reveal the interplay between local (at the scale of a 10s μm) and global (at the scale of a 100s μm) oxidation dynamics. The global electrochemical data and the averaged normalized intensities of reflected light across the entire surface indicated three distinct periods. These periods, backed by a direct correlation between electrochemical and optical data and thermodynamics simulations, were attributed to: (i) the initial covering of the Fe interface with a maghemite layer, (ii) the subsequent transformation of maghemite to magnetite, and (iii) in-depth Fe oxidation. Across all three periods, at a local scale, the absolute magnitude of reactivity consistently followed a polygonal pattern approximately 10 μm in size, a pattern that resembles the crystallographic structure of the metal. Contrastingly, at a macroscopic level, the electrode's proximity to the edge dictates its kinetics and the degree of local oxidation. This research underscores the importance of considering both local and global dynamics in a comprehensive analysis of electroactive interfaces, offering a quantitative framework for optical signal analysis to address this challenge.

Acknowledgements

https://doi.org/10.26434/chemrxiv-2023-stbm1-v3 **ORCID:** https://orcid.org/0000-0003-4289-9678 Content not peer-reviewed by ChemRxiv. **License:** CC BY-NC-ND 4.0

This work was partially financially supported by the Agence Nationale de la Recherche 10 (ANR) Jeunes chercheuses, jeunes chercheurs, ANR JCJC, program (OCTAWA project, ANR-11 22-CE29-0010-01).

References

(1) Li, Y.; Morel, A.; Gallant, D.; Mauzeroll, J. Correlating Corrosion to Surface Grain Orientations of Polycrystalline Aluminum Alloy by Scanning Electrochemical Cell Microscopy. *ACS Appl. Mater. Interfaces* **2022**, *14* (41), 47230–47236. https://doi.org/https://doi.org/10.1021/acsami.2c12813.

(2) Bentley, C. L. Scanning Electrochemical Cell Microscopy for the Study of (Nano)Particle Electrochemistry: From the Sub-Particle to Ensemble Level. *Electrochem. Sci. Adv.* **2022**, *2* (3), e2100081. https://doi.org/10.1002/ELSA.202100081.

(3) Daviddi, E.; Shkirskiy, V.; Kirkman, P. M.; Robin, M. P.; Bentley, C. L.; Unwin, P. R. Screening the Surface Structure-Dependent Action of a Benzotriazole Derivative on Copper Electrochemistry in a Triple-Phase Nanoscale Environment. *J. Phys. Chem. C* **2022**, *126* (35), 14897–14907. https://doi.org/10.1021/acs.jpcc.2c04494.

(4) Daviddi, E.; Gaudin, L. F.; Bentley, C. L. Scanning Electrochemical Cell Microscopy: High-Resolution Structure−property Studies of Mono- and Polycrystalline Electrode Materials. *Curr. Opin. Electrochem.* **2022**, *34*, 101006. https://doi.org/10.1016/j.coelec.2022.101006.

(5) Ryu, C. H.; Lee, H.; Lee, H.; Ren, H. Learning from the Heterogeneity at Electrochemical Interfaces. *J. Phys. Chem. Lett.* **2022**, *13* (33), 7838–7846. https://doi.org/10.1021/ACS.JPCLETT.2C02009/ASSET/IMAGES/MEDIUM/JZ2C02009_0009.GIF.

(6) Shkirskiy, V.; Yule, L. C.; Daviddi, E.; Bentley, C. L.; Aarons, J.; West, G.; Unwin, P. R. Nanoscale Scanning Electrochemical Cell Microscopy and Correlative Surface Structural Analysis to Map Anodic and Cathodic Reactions on Polycrystalline Zn in Acid Media. *J. Electrochem. Soc.* **2020**, *167* (4), 041507. https://doi.org/10.1149/1945-7111/ab739d.

(7) Wang, Y.; Li, M.; Ren, H. Interfacial Structure and Energy Determine the Heterogeneity in the Electrochemical Metal Dissolution Activity at Grain Boundary. *Chem. Mater.* **2023**, *35* (11), 4243–4249. https://doi.org/10.1021/acs.chemmater.3c00220.

(8) Yule, L. C.; Shkirskiy, V.; Aarons, J.; West, G.; Bentley, C. L.; Shollock, B. A.; Unwin, P. R. Nanoscale Active Sites for the Hydrogen Evolution Reaction on Low Carbon Steel. *J. Phys. Chem. C* **2019**, *123* (39), 24146–24155. https://doi.org/10.1021/acs.jpcc.9b07216.

(9) Gaudin, L. F.; Kang, M.; Bentley, C. L. Facet-Dependent Electrocatalysis and Surface

https://doi.org/10.26434/chemrxiv-2023-stbm1-v3 **ORCID:** https://orcid.org/0000-0003-4289-9678 Content not peer-reviewed by ChemRxiv. **License:** CC BY-NC-ND 4.0

Electrochemical Processes on Polycrystalline Platinum. *Electrochim. Acta* **2023**, *450*, 142223. https://doi.org/10.1016/J.ELECTACTA.2023.142223.

(10) Daviddi, E.; Shkirskiy, V.; Kirkman, P. M.; Robin, M. P.; Bentley, C. L.; Unwin, P. R. Nanoscale Electrochemistry in a Copper/Aqueous/Oil Three-Phase System: Surface Structure–Activity-Corrosion Potential Relationships. *Chem. Sci.* **2021**, *12* (8), 3055–3069. https://doi.org/10.1039/D0SC06516A.

(11) Mariano, R. G.; McKelvey, K.; White, H. S.; Kanan, M. W. Selective Increase in CO2 Electroreduction Activity at Grain-Boundary Surface Terminations. *Science (80-.).* **2017**, *358* (6367), 1187–1192. https://doi.org/10.1126/science.aao3691.

(12) Yule, L. C.; Shkirskiy, V.; Aarons, J.; West, G.; Shollock, B. A.; Bentley, C. L.; Unwin, P. R. Nanoscale Electrochemical Visualization of Grain-Dependent Anodic Iron Dissolution from Low Carbon Steel. *Electrochim. Acta* **2020**, *332*, 135267. https://doi.org/10.1016/j.electacta.2019.135267.

(13) Badwe, N.; Chen, X.; Schreiber, D. K.; Olszta, M. J.; Overman, N. R.; Karasz, E. K.; Tse, A. Y.; Bruemmer, S. M.; Sieradzki, K. Decoupling the Role of Stress and Corrosion in the Intergranular Cracking of Noble-Metal Alloys. *Nat. Mater.* **2018**, *17* (10), 887–893. https://doi.org/10.1038/s41563-018-0162-x.

(14) Bernal, M.; Torres, D.; Parapari, S. S.; Čeh, M.; Rožman, K. Ž.; Šturm, S.; Ustarroz, J. A Microscopic View on the Electrochemical Deposition and Dissolution of Au with Scanning Electrochemical Cell Microscopy – Part I. *Electrochim. Acta* **2023**, *445*, 142023. https://doi.org/10.1016/j.electacta.2023.142023.

(15) Daviddi, E.; Chen, Z.; Beam Massani, B.; Lee, J.; Bentley, C. L.; Unwin, P. R.; Ratcliff, E. L. Nanoscale Visualization and Multiscale Electrochemical Analysis of Conductive Polymer Electrodes. *ACS Nano* **2019**, *13* (11), 13271–13284. https://doi.org/10.1021/acsnano.9b06302.

(16) Li, X.; Binnemans, K. Oxidative Dissolution of Metals in Organic Solvents. *Chem. Rev.* **2021**, *121* (8), 4506–4530. https://doi.org/10.1021/acs.chemrev.0c00917.

(17) Kang, S.; Cho, S.; Kang, Y. M. Getting to the Bottom of Transition Metal Dissolution. *Nat. Nanotechnol.* **2023**, *18*, 700–701. https://doi.org/10.1038/s41565-023-01396-1.

(18) Jakab, M. A.; Little, D. A.; Scully, J. R. Experimental and Modeling Studies of the Oxygen Reduction Reaction on AA2024-T3. *J. Electrochem. Soc.* **2005**, *152* (8), B311–B320. https://doi.org/10.1149/1.1949047.

(19) Hayden, S. C.; Chisholm, C.; Eichmann, S. L.; Grudt, R.; Frankel, G. S.; Hanna, B.; Headrick, T.; Jungjohann, K. L. Genesis of Nanogalvanic Corrosion Revealed in Pearlitic Steel. *Nano*

https://doi.org/10.26434/chemrxiv-2023-stbm1-v3 **ORCID:** https://orcid.org/0000-0003-4289-9678 Content not peer-reviewed by ChemRxiv. **License:** CC BY-NC-ND 4.0

Lett. **2022**, *22*, 7087–7093. https://doi.org/https://doi.org/10.1021/acs.nanolett.2c02122.

(20) Zou, N.; Zhou, X.; Chen, G.; Andoy, N. M.; Jung, W.; Liu, G.; Chen, P. Cooperative Communication within and between Single Nanocatalysts. *Nat. Chem.* **2018**, *10* (6), 607–614. https://doi.org/10.1038/s41557-018-0022-y.

(21) Hughes, A. E.; Boag, A.; Glenn, A. M.; McCulloch, D.; Muster, T. H.; Ryan, C.; Luo, C.; Zhou, X.; Thompson, G. E. Corrosion of AA2024-T3 Part II: Co-Operative Corrosion. *Corros. Sci.* **2011**, *53* (1), 27–39. https://doi.org/10.1016/j.corsci.2010.09.030.

(22) Denissen, P. J.; Homborg, A. M.; Garcia, S. J. Interpreting Electrochemical Noise and Monitoring Local Corrosion by Means of Highly Resolved Spatiotemporal Real-Time Optics. *J. Electrochem. Soc.* **2019**, *166* (11), C3275–C3283. https://doi.org/10.1149/2.0341911jes.

(23) Godeffroy, L.; Derouich, S.; Kanoufi, F.; Shkirskiy, V.; Makogon, A.; Derouich, S.; Kanoufi, F.; Shkirskiy, V. Imaging and Quantifying the Chemical Communication between Single Particles in Metal Alloy. *Anal. Chem.* **2023**, *95* (26), 9999–10007. https://doi.org/10.1021/acs.analchem.3c01258.

(24) Tao, B.; McPherson, I. J.; Daviddi, E.; Bentley, C. L.; Unwin, P. R. Multiscale Electrochemistry of Lithium Manganese Oxide (LiMn2O4): From Single Particles to Ensembles and Degrees of Electrolyte Wetting. *ACS Sustain. Chem. Eng.* **2023**, *11* (4), 1459–1471. https://doi.org/10.1021/acssuschemeng.2c06075.

(25) Shkirskiy, V.; Kanoufi, F. Reflective Microscopy for Mechanistic Insights in Corrosion Research. *Curr. Opin. Electrochem.* **2023**, *39*, 101259. https://doi.org/10.1016/j.coelec.2023.101259.

(26) Pfaff, S.; Larsson, A.; Orlov, D.; Harlow, G. S.; Abbondanza, G.; Linpé, W.; Rämisch, L.; Gericke, S. M.; Zetterberg, J.; Lundgren, E. Operando Reflectance Microscopy on Polycrystalline Surfaces in Thermal Catalysis, Electrocatalysis, and Corrosion. *ACS Appl. Mater. Interfaces* **2021**, *13* (16), 19530–19540. https://doi.org/10.1021/acsami.1c04961.

(27) Linpé, W.; Harlow, G. S.; Larsson, A.; Abbondanza, G.; Rämisch, L.; Pfaff, S.; Zetterberg, J.; Evertsson, J.; Lundgren, E. An Electrochemical Cell for 2-Dimensional Surface Optical Reflectance during Anodization and Cyclic Voltammetry. *Rev. Sci. Instrum.* **2020**, *91*, 044101. https://doi.org/10.1063/1.5133905.

(28) Denissen, P. J.; Garcia, S. J. Reducing Subjectivity in EIS Interpretation of Corrosion and Corrosion Inhibition Processes by In-Situ Optical Analysis. *Electrochim. Acta* **2019**, *293*, 514–524. https://doi.org/10.1016/j.electacta.2018.10.018.

(29) Chakri, S.; Patel, A. N.; Frateur, I.; Kanoufi, F.; Sutter, E. M. M.; Tran, T. T. M.; Tribollet, B.;

https://doi.org/10.26434/chemrxiv-2023-stbm1-v3 **ORCID:** https://orcid.org/0000-0003-4289-9678 Content not peer-reviewed by ChemRxiv. **License:** CC BY-NC-ND 4.0

Vivier, V. Imaging of a Thin Oxide Film Formation from the Combination of Surface Reflectivity and Electrochemical Methods. *Anal. Chem.* **2017**, *89* (10), 5303–5310. https://doi.org/10.1021/acs.analchem.6b04921.

(30) Wint, N.; Ansell, P.; Edy, J.; Williams, G.; McMurray, H. N. A Method for Quantifying the Synergistic Inhibitory Effect of Corrosion Inhibitors When Used in Combination: A 'Chromate Generating Coating.' *J. Electrochem. Soc.* **2019**, *166* (15), C580–C588. https://doi.org/10.1149/2.1021914JES/XML.

(31) Kanoufi, F. Electrochemistry and Optical Microscopy. *Encycl. Electrochem.* **2021**, 1–80. https://doi.org/10.1002/9783527610426.BARD030108.

(32) Williams, G.; Kousis, C.; McMurray, N.; Keil, P. A Mechanistic Investigation of Corrosion-Driven Organic Coating Failure on Magnesium and Its Alloys. *npj Mater. Degrad.* **2019**, *3*, 41. https://doi.org/10.1038/s41529-019-0103-4.

(33) Redor, S.; Godeffroy, L.; Rousse, G.; Abakumov, A. M.; Li, B.; Kanoufi, F.; Tarascon, J.-M. Electrochromic Corundum-like Compound Based on the Reversible (De)Insertion of Lithium: Li 2 Ni 2 W 2 O 9. *J. Am. Chem. Soc.* **2023**, *145* (23), 12823–12836. https://doi.org/10.1021/jacs.3c03631.

(34) Godeffroy, L.; Aguilar, I.; Médard, J.; Larcher, D.; Tarascon, J.-M.; Kanoufi, F. Decoupling the Dynamics of Zinc Hydroxide Sulfate Precipitation/Dissolution in Aqueous Zn–MnO 2 Batteries by Operando Optical Microscopy: A Missing Piece of the Mechanistic Puzzle. *Adv. Energy Mater.* **2022**, *12* (30), 2200722. https://doi.org/10.1002/aenm.202200722.

(35) Büchler, M.; Schmuki, P.; Böhni, H. Formation and Dissolution of the Passive Film on Iron Studied by a Light Reflectance Technique. *J. Electrochem. Soc.* **1997**, *144* (7), 2307–2312. https://doi.org/10.1149/1.1837809.

(36) Olgiati, M.; Denissen, P. J.; Garcia, S. J. When All Intermetallics Dealloy in AA2024-T3: Quantifying Early Stage Intermetallic Corrosion Kinetics under Immersion. *Corros. Sci.* **2021**, *192*, 109836. https://doi.org/10.1016/j.corsci.2021.109836.

(37) Larsson, A.; Vorobyova, M.; Pfaff, S.; Abbondanza, G.; Pan, J.; Zetterberg, J.; Lundgren, E. Operando Surface Optical Reflectance Microscopy Study of Corrosion Film Growth on a Ni − Cr − Mo Alloy During Anodic Polarization. *J. Phys. Chem. C* **2023**, *127* (44), 21871–21877. https://doi.org/10.1021/acs.jpcc.3c05984.

(38) Godeffroy, L.; Lemineur, J.-F.; Shkirskiy, V.; Vieira, M. M.; Noël, J.-M.; Kanoufi, F. Bridging the Gap between Single Nanoparticle Imaging and Global Electrochemical Response by Correlative Microscopy Assisted By Machine Vision. *Small Methods* **2022**, *6* (9), 2200659.

https://doi.org/10.26434/chemrxiv-2023-stbm1-v3 **ORCID:** https://orcid.org/0000-0003-4289-9678 Content not peer-reviewed by ChemRxiv. **License:** CC BY-NC-ND 4.0

https://doi.org/10.1002/SMTD.202200659.

(39) Li, R.; Makogon, A.; Galochkina, T.; Lemineur, J.-F.; Kanoufi, F.; Shkirskiy, V. Unsupervised Analysis of Optical Imaging Data for the Discovery of Reactivity Patterns in Metal Alloy. *Small Methods* **2023**, *7* (10), 2300214. https://doi.org/10.1002/smtd.202300214.

(40) Massoud, T.; Maurice, V.; Klein, L. H.; Marcus, P. Nanoscale Morphology and Atomic Structure of Passive Films on Stainless Steel. *J. Electrochem. Soc.* **2013**, *160* (6), C232–C238. https://doi.org/10.1149/2.067306jes.

(41) Rees, E. E.; Ryan, M. P.; McPhail, D. S. An STM Study of the Nanocrystalline Structure of the Passive Film on Iron. *Electrochem. Solid-State Lett.* **2002**, *5* (6), 21–24. https://doi.org/10.1149/1.1475198.

(42) Deng, H.; Nanjo, H.; Qian, P.; Santosa, A.; Ishikawa, I.; Kurata, Y. Potential Dependence of Surface Crystal Structure of Iron Passive Films in Borate Buffer Solution. *Electrochim. Acta* **2007**, *52* (12), 4272–4277. https://doi.org/10.1016/j.electacta.2006.12.005.

(43) Maurice, V.; Marcus, P. Passive Films at the Nanoscale. *Electrochim. Acta* **2012**, *84*, 129–138. https://doi.org/10.1016/j.electacta.2012.03.158.

(44) Ryan, M. P.; Newman, R. C.; Thompson, G. E. An STM Study of the Passive Film Formed on Iron in Borate Buffer Solution. *J. Electrochem. Soc.* **1995**, *142* (10), L177–L179. https://doi.org/10.1149/1.2050035.

(45) Díez-Pérez, I.; Gorostiza, P.; Sanz, F.; Müller, C. First Stages of Electrochemical Growth of the Passive Film on Iron. *J. Electrochem. Soc.* **2001**, *148* (8), B307–B313. https://doi.org/10.1149/1.1381073.

(46) Davenport, A. J.; Oblonsky, L. J.; Ryan, M. P.; Toney, M. F. The Structure of the Passive Film That Forms on Iron in Aqueous Environments. *J. Electrochem. Soc.* **2000**, *147* (6), 2162–2173. https://doi.org/10.1149/1.1393502.

(47) Toney, M. F.; Davenport, A. J.; Oblonsky, L. J.; Ryan, M. P.; Vitus, C. M. Atomic Structure of the Passive Oxide Film Formed on Iron. *Phys. Rev. Lett.* **1997**, *79* (21), 4282–4285. https://doi.org/10.1103/PhysRevLett.79.4282.

(48) https://refractiveindex.info/.

(49) Al-Kuhaili, M. F.; Saleem, M.; Durrani, S. M. A. Optical Properties of Iron Oxide (α-Fe2O3) Thin Films Deposited by the Reactive Evaporation of Iron. *J. Alloys Compd.* **2012**, *521*, 178–182. https://doi.org/10.1016/j.jallcom.2012.01.115.

(50) Batsanov, S. S.; Ruchkin, E. D.; Poroshina, I. A. *Refractive Indices of Solids (SpringerBriefs in*

https://doi.org/10.26434/chemrxiv-2023-stbm1-v3 **ORCID:** https://orcid.org/0000-0003-4289-9678 Content not peer-reviewed by ChemRxiv. **License:** CC BY-NC-ND 4.0

Applied Sciences and Technology), 1st ed.; Springer, 2016.

(51) Go, S.; Lyapustin, A.; Schuster, G. L.; Choi, M.; Ginoux, P.; Chin, M.; Kalashnikova, O.; Dubovik, O.; Kim, J.; Da Silva, A.; Holben, B.; Reid, J. S. Inferring Iron-Oxide Species Content in Atmospheric Mineral Dust from DSCOVR EPIC Observations. *Atmos. Chem. Phys.* **2022**, *22* (2), 1395–1423. https://doi.org/10.5194/acp-22-1395-2022.

(52) Hashimoto, T.; Yamada, T.; Yoko, T. Third-Order Nonlinear Optical Properties of Sol-Gel Derived α-Fe2O3, γ-Fe2O3, and Fe3O4 Thin Films. *J. Appl. Phys.* **1996**, *80* (6), 3184–3190. https://doi.org/10.1063/1.363258.

(53) Tepper, T.; Ross, C. A.; Dionne, G. F. Microstructure and Optical Properties of Pulsed-Laser-Deposited Iron Oxide Films. *IEEE Trans. Magn.* **2004**, *40* (3), 1685–1690. https://doi.org/10.1109/TMAG.2004.827215.

(54) David, R. L. *Handbook of Chemistry and Physics*, 88th ed.; Chemical Rubber Company, 2007.

(55) Puigdomenech, I. Chemical Equilibrium Diagrams https://sites.google.com/site/chemdiagr/home (accessed Jul 6, 2023).

(56) Onderwaater, W. G.; Taranovskyy, A.; Van Baarle, G. C.; Frenken, J. W. M.; Groot, I. M. N. In Situ Optical Reflectance Difference Observations of CO Oxidation over Pd(100). *J. Phys. Chem. C* **2017**, *121* (21), 11407–11415. https://doi.org/10.1021/acs.jpcc.7b02054.

(57) Aspens, D. E. Optical Response of Microscopically Rough Surfaces. *Phys. Rev. B* **1990**, *41* (15), 10334–10343.

(58) Critelli, R. A. J.; Bertotti, M.; Torresi, R. M. Probe Effects on Concentration Profiles in the Diffusion Layer: Computational Modeling and near-Surface PH Measurements Using Microelectrodes. *Electrochim. Acta* **2018**, *292*, 511–521. https://doi.org/10.1016/j.electacta.2018.09.157.

(59) Klymenko, O. V.; Svir, I.; Amatore, C. New Theoretical Insights into the Competitive Roles of Electron Transfers Involving Adsorbed and Homogeneous Phases. *J. Electroanal. Chem.* **2013**, *688*, 320–327. https://doi.org/10.1016/j.jelechem.2012.07.022.

(60) Amatore, C.; Szunerits, S.; Thouin, L.; Warkocz, J. S. The Real Meaning of Nernst's Steady Diffusion Layer Concept under Non-Forced Hydrodynamic Conditions. A Simple Model Based on Levich's Seminal View of Convection. *J. Electroanal. Chem.* **2001**, *500* (1–2), 62–70. https://doi.org/10.1016/S0022-0728(00)00378-8.

(61) Frankel, G. S. Pitting Corrosion of Metals: A Review of the Critical Factors. *J. Electrochem. Soc.* **1998**, *145* (6), 2186–2198.

https://doi.org/10.26434/chemrxiv-2023-stbm1-v3 **ORCID:** https://orcid.org/0000-0003-4289-9678 Content not peer-reviewed by ChemRxiv. **License:** CC BY-NC-ND 4.0

(62) Munteanu, S.; Roger, J. P.; Fedala, Y.; Amiot, F.; Combellas, C.; Tessier, G.; Kanoufi, F. Mapping Fluxes of Radicals from the Combination of Electrochemical Activation and Optical Microscopy. *Faraday Discuss.* **2013**, *164*, 241–258. https://doi.org/10.1039/c3fd00024a.

(63) Jorcin, J.-B.; Blanc, C.; Pébère, N.; Tribollet, B.; Vivier, V. Galvanic Coupling Between Pure Copper and Pure Aluminum. *J. Electrochem. Soc.* **2008**, *155* (1), C46–C51. https://doi.org/10.1149/1.2803506.

(64) Snihirova, D.; Höche, D.; Lamaka, S.; Mir, Z.; Hack, T.; Zheludkevich, M. L. Galvanic Corrosion of Ti6Al4V -AA2024 Joints in Aircraft Environment: Modelling and Experimental Validation. *Corros. Sci.* **2019**, *157*, 70–78. https://doi.org/10.1016/j.corsci.2019.04.036.

(65) Park, H.; Takmakov, P.; Lee, H. Electrochemical Evaluations of Fractal Microelectrodes for Energy Efficient Neurostimulation. *Sci. Rep.* **2018**, *8* (1), 1–11. https://doi.org/10.1038/s41598-018-22545-w.

https://doi.org/10.26434/chemrxiv-2023-stbm1-v3 **ORCID:** https://orcid.org/0000-0003-4289-9678 Content not peer-reviewed by ChemRxiv. **License:** CC BY-NC-ND 4.0

Supporting Information

Deciphering the Interplay between Local and Global Dynamics of Anodic Metal Oxidation

Aleksei Makogon, Jean-Marc Noël, Frédéric Kanoufi, Viacheslav Shkirskiy*

Université Paris Cité, ITODYS, CNRS, 75013 Paris/France

viacheslav.shkirskiy@cnrs.fr

Table of content

https://doi.org/10.26434/chemrxiv-2023-stbm1-v3 **ORCID:** https://orcid.org/0000-0003-4289-9678 Content not peer-reviewed by ChemRxiv. **License:** CC BY-NC-ND 4.0

SI-1 Experimental part

Materials

A rod of > 98% pure Fe, with a diameter of 9.5 mm and a length of 50 cm, was sourced from GoodFellow. This rod was manually sharpened and cut to form an approximate 1 cm cone. The resulting cone was then embedded in a quick-set epoxy adhesive (RS PRO 850-940), allowed to air-dry, and then polished using 320-grit SiC until the Fe surface at the tip of the cone was exposed with the surface area of 0.0015 cm^2. Immediately prior to experimentation, the sample was successively polished using 400, 600, and 1200 grit SiC under tap water cooling. The sample was subsequently cleaned with ethanol and deionized water, gently air-dried, and then placed in the electrochemical cell. All experiments were conducted in aqueous solutions of 5 mM NaCl (analytical grade, VWR Prolabo), prepared using water purified by a MilliporeTM system (18 MΩ×cm).

Reflective microscopy (RM) methodology

Measurement principle

The Fe sample, embedded in epoxy and polished, was fixed at the bottom of a homemade cylindrical cell. This setup exposed a circular area of approximately 50 mm^2. Of this area, only 0.0015 cm^2 was the Fe surface, while the remaining area consisted of the epoxy resin. The cell was then placed into a Reflective Microscopy (RM) setup, with light illumination and collection occurring from the top (Fig. 1a). The Fe electrode was connected as the working electrode at the base of the cell, while the Pt counter and 3.4 M Ag/AgCl reference electrodes were also positioned at the bottom, controlled by a CHI 660A Potentiostat. Further details of the in-house developed RM setup can be found elsewhere.[1,2] Briefly, the setup included an Olympus microscope equipped with a water immersion objective (magnification ×10, 1.00-NA, Olympus LUMPlanFLN W) having a focal distance of approximately 3.5 mm, and an SVCam exo541MU3 CCD camera (SVS-Vistek GmbH, 4496×4504 pixels, 12 bit) operating at 10-25VDC. In this work, we employed binning to reduce the resolution by a factor of 2 in both x and y dimensions, thereby increasing the acquisition rate of the camera. Therefore, the size of each individual pixel was approximately 0.5 µm. A halogen white lamp, filtered at λ = 490 nm blue light using an interference filter (spectral bandwidth of 20 nm), served as the light source. The substrate was top-illuminated by the blue light beam via the microscope objective. The same objective collected the reflected light, directing it to the CCD camera, thus enabling real-time imaging of the light flux reflected by the analyzed surface. Prior to the experiment, we ensured the planarity of the analyzed surface area (with a precision of 10^{-2} degrees) using an interference Mirau objective (magnification ×10 (CF Plan, Nikon)) by minimizing the number of interference fringes over the imaged plane. Next, we gently poured 20 mL of 5 mM NaCl solution into the cell. After making focus adjustments in the optical microscope and measuring the open circuit potential (OCP) for about 5 minutes, we initiated chronoamperometry at a potential of +0.1 V vs OCP. Simultaneously, image

https://doi.org/10.26434/chemrxiv-2023-stbm1-v3 **ORCID:** https://orcid.org/0000-0003-4289-9678 Content not peer-reviewed by ChemRxiv. **License:** CC BY-NC-ND 4.0

acquisition began at a rate of 10 Hz. After 3-6 minutes, we halted the image acquisition and potential application, then removed and repolished the substrate. To ensure the statistical significance of our observations, we repeated the experiment a total of four times.

Data processing

The central concept underpinning our data processing is that the light reflectivity (R) is proportional to both the thickness (δ) and the composition (via its refractive index n) of surface films on metal substrates.[1–5] This principle, rooted in the notion of light interference reflected from the metal interface and surface films (Fig. 1a in the main text), has already been substantiated for flat Fe[2] and Al-based substrates.[1,5] It is derived from the Fresnel equations, the specifics of which can be found in another sources.[1–4] Extensive previous research using *in-situ* STM[6–10] and *in-situ* synchrotron X-ray diffraction[11,12] has suggested that the surface film formed is crystalline and comprises γ-Fe_2O_3 (maghemite) and Fe_3O_4 (magnetite) compounds, dependent on the pH and extent of Fe oxidation. We also considered α-Fe_2O_3 (hematite), a polymorph of maghemite[13–16]. Theoretical variations of reflectivity intensities ($1 + \Delta R/R$) have been plotted in Fig. 2a (main text). The input values for simulations are as follows (for λ = 490 nm): $n_{Fe} = 1.06 + 4.99i$, $n_{Fe_3O_4} = 2.3$, $n_{\gamma-Fe_2O_3} = 2.6$, $n_{\alpha-Fe_2O_3} = 3.2$ $n_{H_2O} = 1.3$.[17–23] To compare the theoretical predictions with experimental values, the intensity of the reflected light ($I(t)$) has been normalized by the light intensity at t=0:

$$\frac{I(t)}{I(t=0)} = 1 + \frac{\Delta R}{R} \quad (1),$$

where t stands for time. Please note that in the main text, we exclusively discuss maghemite and not hematite. This is due to the closer alignment of the theoretical curves for maghemite (in Fig. 3c in the main text), as compared to those for hematite. This determination is based on the Fresnel approximation and the referenced values of refractive indices. All data processing was executed in a Jupyter Lab environment powered by Python 3. The original data and Python code that produced all images in this manuscript are available in the Zenodo repository (https://doi.org/10.5281/zenodo.8341764) under the terms of a Creative Commons Attribution 4.0 International license.

https://doi.org/10.26434/chemrxiv-2023-stbm1-v3 **ORCID:** https://orcid.org/0000-0003-4289-9678 Content not peer-reviewed by ChemRxiv. **License:** CC BY-NC-ND 4.0

SI-2 Computation of chemical equilibrium diagram

A potential-pH diagram for Fe was generated using the HYDRO Medusa Chemical Equilibrium Software to elucidate the observed Fe oxidation behavior.[13] The software-provided potential versus standard hydrogen electrode (SHE) was recalibrated, considering that the potential of a 3.4 M Ag/AgCl solution is -0.2 V relative to SHE.[24] The soluble Fe species considered in the study were Fe^{2+}, $Fe(OH)_2^+$, $Fe(OH)_3$, $Fe(OH)_4^-$, $Fe_2(OH)_2^{4+}$, $Fe_3(OH)_4^{5+}$, FeO_4^{2-}, $FeOH^{2+}$, $Fe(OH)_2$, $Fe(OH)_3^-$, $Fe(OH)_4^{2-}$, $FeOH^+$, $FeCl^{2+}$, $FeCl_2^+$, $FeCl_3$, $FeCl_4^-$ and $FeCl^+$. In addition, the solid Fe species taken into account were $Fe(OH)_3$(s), Fe_2O_3(s), FeOOH(s), $Fe(OH)_2$(s), $Fe_3(OH)_8$(s), and Fe_3O_4(s) and $Fe(OH)_{2.7}Cl_{0.3}$(s). It is important to note that Fe_2O_3(s) can exist in two phases: α (hematite) and γ (maghemite). In the original Pourbaix diagram, only the hematite phase is mentioned.[25] However, recent studies focusing on nanometer-thick passive film formation on Fe suggest that the maghemite phase is actually formed.[6–12] Some authors argue that, in the case of nanometer layers or nanoparticles, the maghemite phase may be more thermodynamically favored than hematite.[26] To account for this, we replaced hematite with maghemite. All equilibrium constants for the given species were used as reported in the software database,[13,27] except for maghemite and $Fe(OH)_{2.7}Cl_{0.3}$(s). For maghemite, we adjusted the equilibrium constant (K) to account for a deviation in the reported values of its Gibbs free energy of formation,[14,26–28] thereby ensuring a better correlation with the results reported in our study. We set the lg$K$ of the reaction

$$2Fe^{3+} + 3H_2O \leftrightarrow 6H^+ + Fe_2O_3(s) \quad (2)$$

to -1.5, in accordance with the notation used in the Hydro Meduza Database entries.[13] We also adjusted the K value for $Fe(OH)_{2.7}Cl_{0.3}$(s) formation from 3.0 (as reported in the Hydro Meduza database) to 1.0 (as used in this study), significantly suppressing its formation. This is consistent with literature reports indicating suppression of Cl-containing Fe corrosion products at the low Cl concentrations we utilized.[29] The calculation was conducted at a temperature of 25 ºC, with the total concentration of Fe species held at 0.1 M, and a NaCl concentration of 5 mM.

https://doi.org/10.26434/chemrxiv-2023-stbm1-v3 **ORCID:** https://orcid.org/0000-0003-4289-9678 Content not peer-reviewed by ChemRxiv. **License:** CC BY-NC-ND 4.0

References

(1) Godeffroy, L.; Derouich, S.; Kanoufi, F.; Shkirskiy, V.; Makogon, A.; Derouich, S.; Kanoufi, F.; Shkirskiy, V. Imaging and Quantifying the Chemical Communication between Single Particles in Metal Alloy. *Anal. Chem.* **2023**, *95* (26), 9999–10007. https://doi.org/10.1021/acs.analchem.3c01258.

(2) Chakri, S.; Patel, A. N.; Frateur, I.; Kanoufi, F.; Sutter, E. M. M.; Tran, T. T. M.; Tribollet, B.; Vivier, V. Imaging of a Thin Oxide Film Formation from the Combination of Surface Reflectivity and Electrochemical Methods. *Anal. Chem.* **2017**, *89* (10), 5303–5310. https://doi.org/10.1021/acs.analchem.6b04921.

(3) Lemineur, J.-F.; Wang, H.; Wang, W.; Kanoufi, F. Emerging Optical Microscopy Techniques for Electrochemistry. *Annu. Rev. Anal. Chem.* **2022**, *15* (1), 57–82. https://doi.org/10.1146/annurev-anchem-061020-015943.

(4) Kanoufi, F. Electrochemistry and Optical Microscopy. *Encycl. Electrochem.* **2021**, 1–80. https://doi.org/10.1002/9783527610426.BARD030108.

(5) Li, R.; Makogon, A.; Galochkina, T.; Lemineur, J.-F.; Kanoufi, F.; Shkirskiy, V. Unsupervised Analysis of Optical Imaging Data for the Discovery of Reactivity Patterns in Metal Alloy. *Small Methods* **2023**, *7* (10), 2300214. https://doi.org/10.1002/smtd.202300214.

(6) Rees, E. E.; Ryan, M. P.; McPhail, D. S. An STM Study of the Nanocrystalline Structure of the Passive Film on Iron. *Electrochem. Solid-State Lett.* **2002**, *5* (6), 21–24. https://doi.org/10.1149/1.1475198.

(7) Deng, H.; Nanjo, H.; Qian, P.; Santosa, A.; Ishikawa, I.; Kurata, Y. Potential Dependence of Surface Crystal Structure of Iron Passive Films in Borate Buffer Solution. *Electrochim. Acta* **2007**, *52* (12), 4272–4277. https://doi.org/10.1016/j.electacta.2006.12.005.

(8) Maurice, V.; Marcus, P. Passive Films at the Nanoscale. *Electrochim. Acta* **2012**, *84*, 129–138. https://doi.org/10.1016/j.electacta.2012.03.158.

(9) Ryan, M. P.; Newman, R. C.; Thompson, G. E. An STM Study of the Passive Film Formed on Iron in Borate Buffer Solution. *J. Electrochem. Soc.* **1995**, *142* (10), L177–L179. https://doi.org/10.1149/1.2050035.

(10) Díez-Pérez, I.; Gorostiza, P.; Sanz, F.; Müller, C. First Stages of Electrochemical Growth of the Passive Film on Iron. *J. Electrochem. Soc.* **2001**, *148* (8), B307–B313. https://doi.org/10.1149/1.1381073.

(11) Davenport, A. J.; Oblonsky, L. J.; Ryan, M. P.; Toney, M. F. The Structure of the Passive Film That Forms on Iron in Aqueous Environments. *J. Electrochem. Soc.* **2000**, *147* (6), 2162–2173. https://doi.org/10.1149/1.1393502.

(12) Toney, M. F.; Davenport, A. J.; Oblonsky, L. J.; Ryan, M. P.; Vitus, C. M. Atomic Structure of the Passive Oxide Film Formed on Iron. *Phys. Rev. Lett.* **1997**, *79* (21), 4282–4285. https://doi.org/10.1103/PhysRevLett.79.4282.

(13) Puigdomenech, I. Chemical Equilibrium Diagrams https://sites.google.com/site/chemdiagr/home (accessed Jul 6, 2023).

(14) Majzlan, J.; Grevel, K.-D.; Navrotsky, A. Thermodynamics of Fe Oxides: Part II. Enthalpies of Formation and Relative Stability of Goethite (α-FeOOH), Lepidocrocite (γ-FeOOH), and Maghemite (γ-Fe2O3). *Am. Mineral.* **2003**, *88*, 855–859. https://doi.org/https://doi.org/10.2138/am-2003-5-614.

https://doi.org/10.26434/chemrxiv-2023-stbm1-v3 **ORCID:** https://orcid.org/0000-0003-4289-9678 Content not peer-reviewed by ChemRxiv. **License:** CC BY-NC-ND 4.0

(15) Nasrazadani, S.; Raman, A. Formation and Transformation of Magnetite (Fe3O4) on Steel Surfaces under Continuous and Cyclic Water Fog Testing. *Corrosion* **1993**, *49* (4), 294–300. https://doi.org/10.5006/1.3316052.

(16) Bernabale, M.; Cognigni, F.; Nigro, L.; Rossi, M.; de Caro, T.; De Vito, C. A Comprehensive Strategy for Exploring Corrosion in Iron-Based Artefacts through Advanced Multiscale X-Ray Microscopy. *Sci. Rep.* **2022**, *12* (1), 1–9. https://doi.org/10.1038/s41598-022-10151-w.

(17) https://refractiveindex.info/.

(18) Al-Kuhaili, M. F.; Saleem, M.; Durrani, S. M. A. Optical Properties of Iron Oxide (α-Fe2O3) Thin Films Deposited by the Reactive Evaporation of Iron. *J. Alloys Compd.* **2012**, *521*, 178–182. https://doi.org/10.1016/j.jallcom.2012.01.115.

(19) Batsanov, S. S.; Ruchkin, E. D.; Poroshina, I. A. *Refractive Indices of Solids (SpringerBriefs in Applied Sciences and Technology)*, 1st ed.; Springer, 2016.

(20) Go, S.; Lyapustin, A.; Schuster, G. L.; Choi, M.; Ginoux, P.; Chin, M.; Kalashnikova, O.; Dubovik, O.; Kim, J.; Da Silva, A.; Holben, B.; Reid, J. S. Inferring Iron-Oxide Species Content in Atmospheric Mineral Dust from DSCOVR EPIC Observations. *Atmos. Chem. Phys.* **2022**, *22* (2), 1395–1423. https://doi.org/10.5194/acp-22-1395-2022.

(21) Hashimoto, T.; Yamada, T.; Yoko, T. Third-Order Nonlinear Optical Properties of Sol-Gel Derived α-Fe2O3, γ-Fe2O3, and Fe3O4 Thin Films. *J. Appl. Phys.* **1996**, *80* (6), 3184–3190. https://doi.org/10.1063/1.363258.

(22) Tepper, T.; Ross, C. A.; Dionne, G. F. Microstructure and Optical Properties of Pulsed-Laser-Deposited Iron Oxide Films. *IEEE Trans. Magn.* **2004**, *40* (3), 1685–1690. https://doi.org/10.1109/TMAG.2004.827215.

(23) David, R. L. *Handbook of Chemistry and Physics*, 88th ed.; Chemical Rubber Company, 2007.

(24) Chowdhury, D. R.; Spiccia, L.; Amritphale, S. S.; Paul, A.; Singh, A. A Robust Iron Oxyhydroxide Water Oxidation Catalyst Operating under near Neutral and Alkaline Conditions. *J. Mater. Chem. A* **2016**, *4* (10), 3655–3660. https://doi.org/10.1039/c6ta00313c.

(25) Pourbaix, M. *Atlas d'équilibres Électrochimique à 25 °C*; Gauthier-Villars, 1963.

(26) Navrotsky, A.; Mazeina, L.; Majzlan, J. Size-Driven Structural and Thermodynamic Complexity in Iron Oxides. *Science (80-.).* **2008**, *319* (5870), 1635–1638. https://doi.org/10.1126/science.1148614.

(27) Beverskog, B.; Puigdomenech, I. Revised Diagrams for Iron At 25-300 ° C. *Corros. Sci.* **1996**, *38* (12), 2121–2135.

(28) Chase, M. W. J. Phys. Chem. Ref. Data, Monograph 9. In *NIST-JANAF Themochemical Tables, Fourth Edition*; 1998; pp 1–1951.

(29) Song, Y.; Jiang, G.; Chen, Y.; Zhao, P.; Tian, Y. Effects of Chloride Ions on Corrosion of Ductile Iron and Carbon Steel in Soil Environments. *Sci. Rep.* **2017**, *7* (1). https://doi.org/10.1038/s41598-017-07245-1.

https://doi.org/10.26434/chemrxiv-2023-stbm1-v3 **ORCID:** https://orcid.org/0000-0003-4289-9678 Content not peer-reviewed by ChemRxiv. **License:** CC BY-NC-ND 4.0